

PHOTONICS Research

Epitaxial indium antimonide for multiband photodetection from IR to millimeter/terahertz wave

JINCHAO TONG,^{1,4}  HENG LUO,² FEI SUO,¹  TIANNING ZHANG,¹ DAWEI ZHANG,³  AND DAO HUA ZHANG^{1,*}

¹School of Electrical and Electronic Engineering, Nanyang Technological University, Singapore 639798, Singapore

²School of Physics and Electronics, Central South University, Changsha 410083, China

³Ministry of Education and Shanghai Key Laboratory of Modern Optical System, University of Shanghai for Science and Technology, Shanghai 200093, China

⁴e-mail: jctong64@163.com

*Corresponding author: edhzhang@ntu.edu.sg

Received 27 September 2021; revised 4 March 2022; accepted 6 March 2022; posted 7 March 2022 (Doc. ID 444354); published 14 April 2022

Conventional photodetection converts light into electrical signals only in a single electromagnetic waveband. Multiband detection technology is highly desirable because it can handle multispectral information discrimination, identification, and processing. Current epitaxial solid-state multiband detection technologies are mainly within the IR wave range. Here, we report epitaxial indium antimonide on gallium arsenide for IR and millimeter/terahertz wave multiband photodetection. The photoresponse originates from interband transition in optoelectrical semiconductors for IR wave, and surface plasmon polaritons induced nonequilibrium electrons for a millimeter/terahertz wave. The detector shows a strong response for an IR wave with a cutoff wavelength of 6.85 μm and a blackbody detectivity of 1.8×10^9 Jones at room temperature. For a millimeter/terahertz wave, the detector demonstrates broadband detection from 0.032 THz (9.4 mm) to 0.330 THz (0.9 mm); that is, from K_a to the W and G bands, with a noise equivalent power of 1.0×10^{-13} $\text{W Hz}^{-1/2}$ at 0.270 THz (1.1 mm) at room temperature. The detection performance is an order of magnitude better while decreasing the temperature to 170 K, the thermoelectric cooling level. Such detectors, capable of large scale and low cost, are promising for advanced uncooled multiband detection and imaging systems. © 2022 Chinese Laser Press

<https://doi.org/10.1364/PRJ.444354>

1. INTRODUCTION

Photodetection converts light into an electrical signal, which can help to acquire spectral information radiated or scattered from objectives. Conventional solid-state photodetectors are usually only able to deal with spectral information within a single electromagnetic waveband due to the existence of a characteristic energy gap that quantum photons must overcome. A multiband detection capability is highly desirable because it can conduct multispectral information discrimination, identification, and processing. The current development of multiband epitaxial solid-state detectors mainly focuses on detector technologies such as HgCdTe, quantum well IR photodetectors (QWIPs), antimonide-based type-II superlattices, and quantum dot IR photodetectors (QDIPs) [1]. However, these technologies only target short-wavelength IR (SWIR) to middle-wavelength IR (MWIR) and long-wavelength IR (LWIR). It is still quite hard to use them for millimeter/terahertz wave detection [2–6] due to the extremely low quantum energy of millimeter/terahertz photons, which, on the one hand, limits the carriers' transition in

conventional optoelectrical semiconductors; on the other hand, it is vulnerable to strong background thermal disturbance.

Thermal-detection is a strategy to realize multispectral band detection. For example, VO_2 - and MCNO-based detectors have demonstrated broad spectral band detection in different wavelength ranges [7]. Some optoelectrical visible or IR semiconductors, such as Si and Ge, also show a significant thermal-response signal for long wavelength millimeter/terahertz waves, but they must be operated at low temperatures [8]. Another widely used broad spectral band thermal detector is the Golay cell, which has a noise equivalent power (NEP) of 10^{-10} – 10^{-9} $\text{W Hz}^{-1/2}$ from IR to millimeter/terahertz [9]. However, it suffers from a bulky configuration and is difficult to extend to large arrays. Generally, thermal detection technologies suffer from slow response (on the order of 10^{-3} s), leading to a lower signal processing speed. In the past decade, graphene and some other novel 2D thin-film materials also have shown the potential to realize broad spectral band photodetection, but

they are usually based on mechanically transferred small-area flakes and the stability in air is still a big challenge [10,11].

Indium antimonide (InSb) is a III-V group semiconductor that has a bandgap of ~ 0.17 eV at room temperature, which enables its use for IR wave detection from intrinsic absorption. Well-grown, high-quality InSb has high electron mobility and a low effective electron mass. These characters give it negative permittivity in the long wavelength millimeter/terahertz wave range, according to the Drude model. This is like gold or silver in UV or visible range, which can help to excite strong light-matter interaction by introducing surface plasmon polaritons (SPPs). SPPs are electromagnetic waves that travel along a metal-dielectric or metal-air interface, practically in the IR or visible frequency range. So, in the long wavelength millimeter and terahertz wave range, they travel along the plasmonic semiconductor-air interface. InSb can be used as an essential platform to develop an SPP-related novel device in the millimeter/terahertz wave range, which opens a new avenue to explore novel optoelectrical components based on InSb [12–16].

One of the outstanding capabilities of plasmonic InSb under the radiation of a millimeter/terahertz wave is that the decay of SPPs can boost the generation of nonequilibrium electrons [17–22]. As a result, a new strategy to realize the detection of long wavelength millimeter/terahertz photons has been proposed [23,24]. In an antenna-coupled ohmic metal-semiconductor-metal configuration, SPPs will be excited in the plasmonic semiconductor under the illumination of a millimeter/terahertz wave. The decay of SPPs then induces nonequilibrium electrons that can form a photocurrent/photovoltage under an external bias. This strategy based on SPPs in semiconductors opens a new avenue to develop sensitive millimeter/terahertz wave detectors.

Here, we report an epitaxially grown InSb on a GaAs substrate for multiband photodetection from the IR to a millimeter/terahertz wave. InSb is a III-V group semiconductor with a bandgap of ~ 0.17 eV at room temperature, which enables its use for IR wave detection based on intrinsic absorption. Well-grown, high-quality InSb has high electron mobility and low effective electron mass, which ensure a fast carrier transition and high optical absorption. Therefore, it is a very good material for IR detection. For a millimeter/terahertz wave, InSb has negative permittivity, and can be used as a very good platform for the excitation of SPPs. The decay of SPPs can induce nonequilibrium electrons, which will then form a photocurrent under external bias. Therefore, it also can be used as a material for millimeter/terahertz wave detection. Because the negative permittivity of InSb can hold up to 3 THz, with appropriate antenna design it can help to realize broad spectral band detection in the millimeter/terahertz wave range. On the other hand, the high electron mobility can ensure sufficient and fast collection of nonequilibrium electrons. Based on reasons mentioned above, InSb is a good material for multiband detection. The multiband detector is equipped with a log-period antenna to couple a millimeter/terahertz wave into an active InSb element. The detection capability of the detector is characterized in detail for multiband. It shows a 100% cutoff wavelength of $6.85 \mu\text{m}$ and $6.44 \mu\text{m}$, respectively, at 293 K and 170 K for an IR wave. At 293 K, the IR blackbody responsivity

and detectivity are $5.4 \times 10^3 \text{ V W}^{-1}$ and 1.8×10^9 Jones, respectively. The corresponding performance can be increased to $4.2 \times 10^4 \text{ V W}^{-1}$ and 8.5×10^9 Jones, respectively, at 170 K. The detector shows a response speed of 8.2×10^{-7} s in the IR. For a millimeter/terahertz wave, it demonstrates multiple spectral band detection from $0.032\text{--}0.040$ THz (K_a band) to $0.075\text{--}0.110$ THz (W band), and to $0.150\text{--}0.330$ THz (G band). At 0.270 THz, the responsivity and NEP are $5.6 \times 10^4 \text{ V W}^{-1}$ and $1.0 \times 10^{-13} \text{ W Hz}^{-1/2}$, respectively, which can be increased to $5.4 \times 10^5 \text{ V W}^{-1}$ and $1.0 \times 10^{-14} \text{ W Hz}^{-1/2}$ at 170 K. A moderate response speed of 1.5×10^{-5} s is achieved for a millimeter/terahertz wave at room temperature.

2. EXPERIMENTAL METHODS

A. Device Design and Simulation

The epitaxial structure was grown on a GaAs substrate by molecular beam epitaxy (MBE). As shown in Fig. 1(a), it

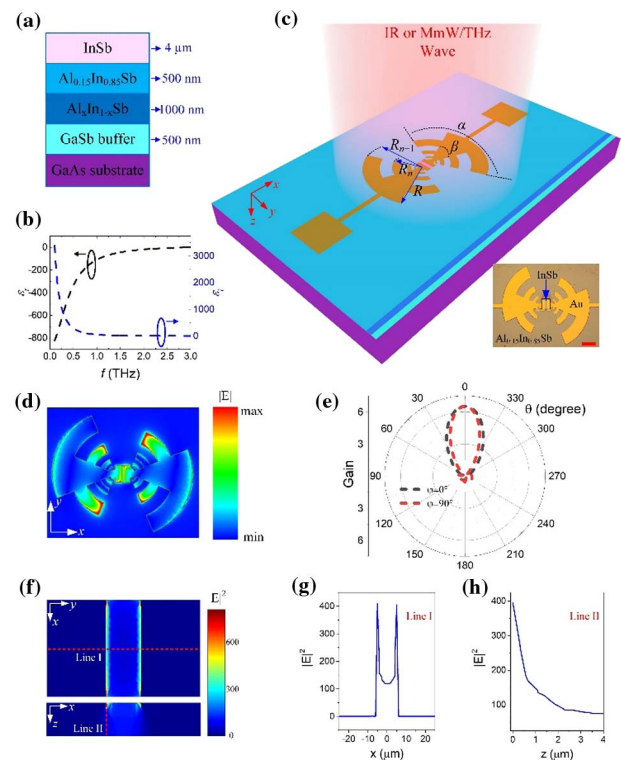


Fig. 1. Design of the epitaxial IR-millimeter/THz wave multiband photodetector. (a) Structure of the epitaxial InSb on GaAs. (b) Relative permittivity of InSb in the millimeter/terahertz wave range followed by a Drude model. (c) Schematic of the multiband detector. A planar log-period antenna is adopted to couple the millimeter/terahertz wave. IR wave impinges on the surface of the InSb mesa. Inset is the microscope image of the detector and the scale bar represents $50 \mu\text{m}$. (d) Typical field distribution by the couple of the antenna calculated by Ansys HFSS software. In the Ansys HFSS antenna simulation, the electromagnetic wave is fed at the gap with an impedance of 50Ω . (e) E plane and H plane of the antenna. (f) Typical distribution of $|E|^2$ near the central Au-InSb-Au structure calculated by COMSOL Multiphysics software. PML boundary condition is adopted in the simulation. The incident light is polarized along the direction of the y axis to meet the experiments. Distribution of $|E|^2$ along (g) the cut-line I and (h) the cut-line II in (f).

contains a GaSb buffer layer (500 nm), an $\text{Al}_{1-x}\text{In}_x\text{Sb}$ graded layer (1000 nm), an $\text{Al}_{0.15}\text{In}_{0.85}\text{Sb}$ barrier layer (500 nm), and an InSb active layer (4 μm) from bottom to top. The thickness of the active InSb layer here is designed larger than that (2 μm) in Ref. [24] because a thicker InSb can guarantee more IR absorption. The relative permittivity of InSb in the millimeter/terahertz range can be described by the Drude model as $\epsilon(\omega) = \epsilon_0 - \omega_p^2/(\omega^2 + i\omega\tau^{-1})$, where ϵ_0 is the static dielectric constant, which is 16.8; ω_p is the plasma frequency; ω is the angular frequency; and τ is the relaxation time of the electrons. ω_p is determined by $\omega_p^2 = q^2n/(m^*\epsilon_0)$, where q is the elementary charge; n is the electron density; m^* is the effective electron mass at the bottom of the band edge, which is $0.014m_0$ for InSb; and ϵ_0 is the permittivity in vacuum. The mobility of the carriers is related to the relaxation time by $\mu = q\tau/m^*$. The electron concentration and mobility of InSb are $2.86 \times 10^{16} \text{ cm}^{-3}$ and $5.0 \times 10^4 \text{ cm}^2 \text{ V}^{-1} \text{ s}^{-1}$, respectively, at room temperature. The calculated relative permittivity of InSb in the millimeter/terahertz wave range is presented in Fig. 1(b). It has negative permittivity (real part) up to ~ 3 THz or in a wavelength down to 0.1 mm at room temperature; for example, the real part of the relative permittivity is -334.6 at 0.5 THz. This makes InSb an ideal plasmonic semiconductor in the millimeter/terahertz wave range. This nature of InSb is like the plasmonic nature of gold or silver in the UV or visible range. Therefore, InSb can be used as a good platform to excite SPPs in the millimeter/terahertz wave range. One of the outstanding characteristics in plasmonic InSb is the generation of nonequilibrium electrons induced by the decay of SPPs. Under an external voltage bias, the photocurrent/photovoltage will be formed between the two terminals of InSb [23].

The design and microscope image of the multiband detector are shown in Fig. 1(c). A metallic planar log-period antenna [25,26] is used to couple a millimeter/terahertz wave to the central active InSb mesa. In the design of this antenna, the geometric ratio is $\tau = R_{n+1}/R_n = 1.4$, the maximum radius is $R = 0.23 \text{ mm}$, and characteristic angles are $\beta = 45^\circ$ and $\alpha = 135^\circ$. The couple capability of the antenna is calculated by Ansys HFSS software. As shown in Fig. 1(d), it can efficiently couple the incident millimeter/terahertz wave into the central gap of the antenna. The typical radiation pattern shows that the antenna can offer the largest gain under normal incidence ($\theta = 0^\circ$). Figure 1(e) plots the gain of the antenna in both the E plane and H plane. A typical antenna G of ~ 7 is achieved by the log-period antenna. The antenna calculation also shows that it can help to couple a millimeter/terahertz wave in a broad spectral band range from 0.03 to 0.34 THz. To gain insight into the generation of SPPs in InSb, we also used COMSOL Multiphysics software to simulate the distribution of $|E|^2$ near the central Au-InSb-Au structure. As shown in Fig. 1(f), strong SPPs can be generated in InSb, resulting in more nonequilibrium electrons. Figures 1(g) and 1(h) plot the distribution of $|E|^2$ along the cut line I and II in Fig. 1(f), respectively. As shown, the intensity of the SPPs has a maximum value at the edge of InSb and gradually declines toward the central part of InSb due to the loss. It also declines along the direction of z . The characteristics of SPPs here agree well with previous reports on SPPs' generation in InSb [12–16].

B. Device Fabrication and Characterization

In detector fabrication, the mesa was formed by a chemical solution ($\text{HF}:\text{H}_2\text{O}_2:\text{citric acid}:\text{DIH}_2\text{O}$) after first photolithography. Next, metallic contacts and a planar antenna (300 nm Au followed by 20 nm Ti adhesion layer) were defined via photolithography, e-beam evaporation, and a standard lift-off process. After being mounted into a ceramic chip and wire-bonded to metallic pads, the detector was fixed in a low temperature Dewar. Current–voltage characteristics were measured with a Keithley 2450 source meter (Tektronix, Beaverton, OR, USA). The Spectral response of the detector for an IR wave was measured using a standard Fourier transform IR spectroscopy (FTIR) system. A standard thermal DTGS detector with a flat response was used for calibration. A 1000 K blackbody source was used to evaluate the blackbody responsivity and specific detectivity for IR wave with a modulation rate of 3 kHz and a field of view π . The blackbody responsivity R_v can be expressed as $R_v = V_{\text{ph}}/P$, where V_{ph} is the photovoltage and P is the incident radiation power on the detector. To determine P , we can use the expression $P = \sigma(T_b^4 - T_0^4)A_b \cdot A/(2\sqrt{2}\pi L^2)$, where σ is the Stefan constant; T_b and T_0 are the temperature of blackbody and background, respectively; A_b is the area of the exit window of the blackbody source; A is the area of the detector; and L is the distance between the detector and the exit window. We also used a standard power meter (Photonics Group, Ophir Optonics) to calibrate the irradiance of the blackbody source. The blackbody detectivity D^* can be calculated as $D^* = R_v(A\Delta f)^{1/2}/v_n$, where Δf is the equivalent noise bandwidth and v_n is the noise voltage. A 2.94 μm laser source with a maximum modulation frequency of 1 MHz was used to obtain the response waveform and $f_{-3\text{dB}}$ value of the detector in IR.

A commercial Virginia Diodes tunable synthesizer (0.008–0.020 THz), a WR28SGX (signal generator extension module 0.026–0.040 THz), a WR10SGX-M (mini signal generator extension module 0.075–0.110 THz), a WR5.1 \times 2 broadband doubler (0.150–0.220 THz), a WR3.4 \times 3 broadband tripler (0.225–0.330 THz), and a PIN switch for fast modulation of the output were used to characterize the performance of the detector for a millimeter/terahertz wave. Four horn antennas were used for four millimeter/terahertz wavebands: WR10CH conical horn antenna (0.075–0.110 THz), WR5.1CH conical horn antenna (0.150–0.220 THz), WR3.4DH diagonal horn antenna (0.225–0.330 THz), and WR28CH conical horn antenna (0.026–0.040 THz). The output radiation power in free space was calibrated by a Goly cell. The responsivity of the detector in a millimeter/terahertz wave can be expressed as $R = V/(pA_e) = V A_G R_G/(V_G A_e)$, where p is the power density; V and V_G are the photovoltage of the detector and Goly cell, respectively; A_e is the effective absorption area of the detector for a millimeter/terahertz wave, described as $A_e = G\lambda^2/(4\pi)$, and G is the gain of the antenna and assumed to be matched to its load; A_G is the absorption area of the Goly cell (50 mm^2); and R_G is the responsivity of the Goly cell ($\sim 10^5 \text{ V W}^{-1}$ at 15 Hz and room temperature). From the perspective of a real application, the figure of merit used to evaluate the performance of a detector for a millimeter/terahertz wave is the noise equivalent power (NEP), which corresponds to the lowest detectable power in a 1 Hz bandwidth. The lower the NEP, the better the performance

of the detector. NEP can be expressed as $NEP = v_n/R$, where v_n is the rms of the noise voltage, and R is the voltage responsivity of the detector.

3. RESULTS

A. Current–Voltage Characterization

Figure 2(a) plots the measured current–voltage (I – V) characteristic curves of the detector at temperatures from 293 to 170 K. They show good linear and symmetric characters, demonstrating good Au/Ti–InSb ohmic contacts in the detector and, therefore, excluding the potential disturbance of a Schottky barrier in the photodetection. The resistance of the detector is found to be increased from 120 Ω at 293 K to 430 Ω at 170 K. This agrees with the variation trend for normal semiconductors. For our detector, in addition to the thermal Johnson–Nyquist noise (v_t), the noise (v_b) due to bias (dark current) should also be included. The total noise can be expressed as $v_n = (v_t^2 + v_b^2)^{1/2} = (4k_B T r + 2q I_d r^2)^{1/2}$ [27–29], where k_B is the Boltzmann’s constant in joule per kelvin, T is the detector’s absolute temperature in kelvin, r is the resistance value of the device in ohm (Ω), q is the elementary charge, and I_d is the dark current of the detector (the bias current in our case). Figure 2(b) plots the noise of the detector at different biases derived from the measured I – V in Fig. 2(a). The increment of noise at higher bias is due to the rising of dark current shot noise v_b . It is noted here that the $1/f$ noise in our measurement can be neglected because we would characterize our detector at high modulation frequency for both IR and millimeter/terahertz waves [30,31]. The typical noise level of our detector is $\sim 10^{-9}$ V Hz^{1/2}.

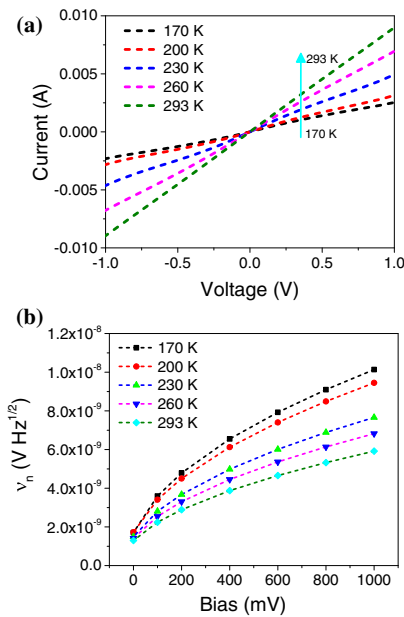


Fig. 2. Dark current and noise of the detector. (a) Current–voltage (I – V) characteristic curves of the detector at temperatures from 293 to 170 K. (b) Calculated voltage noise of the detector with respect to bias at different temperatures.

B. Photoresponse for IR Band

Figure 3(a) shows the relative spectral responses of the detector for an IR wave at different temperatures. At 293 K, it has a long wavelength 100% cutoff at 6.85 μm , which shows a blueshift to 6.44 μm while decreasing the temperature to 170 K. The shift of the cutoff wavelength follows that of the bandgap of InSb. Figure 3(b) shows that blackbody responsivity increases with an increase in the bias at different temperatures. As for the IR wave, the detector here is actually a photoconductor and its responsivity can be expressed as [1] $R_v = q\eta\tau V_b \mu_e / (l^2 h\nu)$, where q is the element charge, η is the quantum efficiency, V_b is the bias voltage, τ is the lifetime of the carriers, μ_e is the mobility of the electrons, and l is the distance between metal contacts. At a relative low bias, the responsivity increases linearly with respect to the bias. However, at relative higher bias, it tends to saturate due to the gradually saturated velocity for carriers. For room temperature operation, the detector has a responsivity of 5.4×10^3 V W⁻¹ at 1000 mV, which is increased to 1.5×10^4 V W⁻¹, 2.6×10^4 V W⁻¹, 3.8×10^4 V W⁻¹, and 4.2×10^4 V W⁻¹, while decreasing the temperature, respectively, to 260 K, 230 K, 200 K, and 170 K, as shown in Fig. 3(c). This increment can be mainly ascribed to the prolonged lifetime and increased mobility at low temperatures [1]. As shown in Fig. 3(d), the detector has a blackbody detectivity of 1.8×10^9 Jones at room temperature at 1000 mV. By decreasing the temperature, the corresponding detectivity can be increased to 4.5×10^9 Jones, 6.9×10^9 Jones, 8.1×10^9 Jones, and 8.5×10^9 Jones at 260 K, 230 K, 200 K, and 170 K, respectively, as shown in Fig. 3(e), mainly owing to the increased responsivity. The performance of our InSb detector for IR is comparable to commercial solid-state InSb, InAsSb, and MCT photoconductors [32–34].

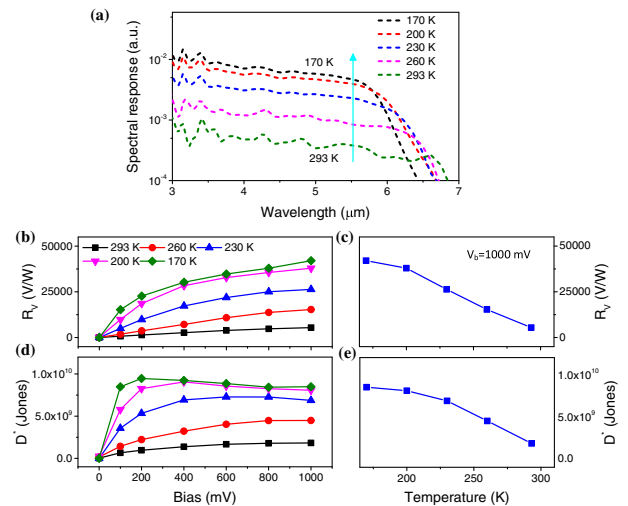


Fig. 3. Characterization of the detector for IR wave detection. (a) Relative spectral response of the detector at different temperatures. (b) Blackbody responsivity of the detector with respect to bias at different temperatures. (c) Blackbody responsivity of the detector at different temperatures under an applied voltage bias of 1000 mV. (d) Blackbody detectivity of the detector with respect to bias at different temperatures. (e) Blackbody detectivity of the detector at different temperatures under an applied voltage bias of 1000 mV.

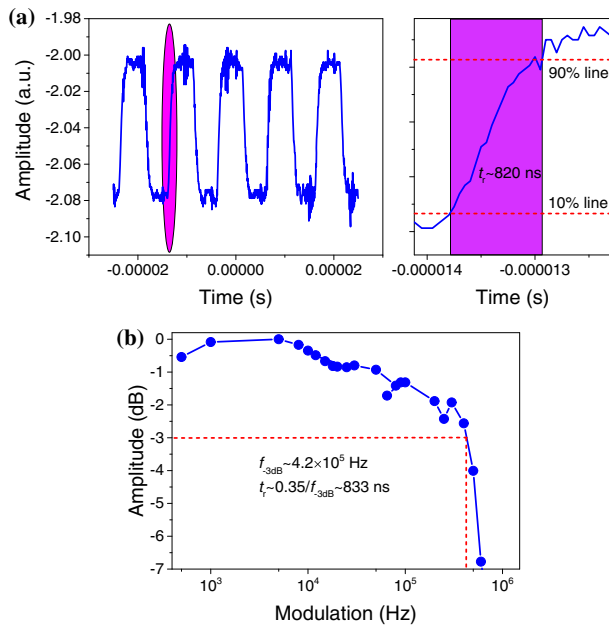


Fig. 4. Response speed of the detector for IR. (a) Typical response waveform of the detector under illumination of a 2.94 μm laser with rise time of 20 ns. (b) Normalized amplitude frequency response of the detector.

To evaluate the response speed of the detector for an IR wave, a 2.94 μm laser source with maximum modulation frequency up to 1 MHz is used to pump the detector. The rise time of the square wave source is 20 ns. The output power of the source is found to be stable to ensure reliable measurements. Figure 4(a) shows the typical response waveform of the detector at room temperature. A rise time as fast as 800 ns (or 8.0×10^{-7} s) is achieved for the InSb photoconductor. We also conducted an amplitude frequency measurement for the detector. As shown in Fig. 4(b), the $f_{-3\text{dB}}$ of the detector is approximately 4.2×10^5 Hz, corresponding to a rise time of 833 ns according to $t_r = 0.35/f_{-3\text{dB}}$, which agrees with that in the time-domain measurement in Fig. 4(a). The achieved response speed is comparable to a commercial counterpart [32].

C. Photoresponse for Millimeter/Terahertz Bands

The performance of our detector was also characterized for a millimeter/terahertz wave. Figure 5(a) shows the measured R_v and NEP of the detector with respect to voltage bias for room temperature operation at 0.270 THz (1.1 mm), where our detector exhibits the best performance over 0.032–0.330 THz. As shown, R_v increases linearly with the voltage bias because the number of nonequilibrium electrons collected by the electrodes is proportional to the drift velocity [23]. At 1000 mV, the R_v and NEP of the detector are 5.6×10^4 V W $^{-1}$ and 1.0×10^{-13} W Hz $^{-1/2}$, respectively. Such a high R_v is comparable to that of a thermal Golay cell (1×10^5 V W $^{-1}$) [9] and a dual-gated bilayer graphene hot electron bolometer operated at 5 K (1×10^5 V W $^{-1}$) [35]. The corresponding NEP shows improvement while increasing bias, but due to increment of noise level, as shown in Fig. 2, it tends to saturate at a relatively large bias of 1000 mV. It demonstrates an order of magnitude improvement compared to the commercially available zero

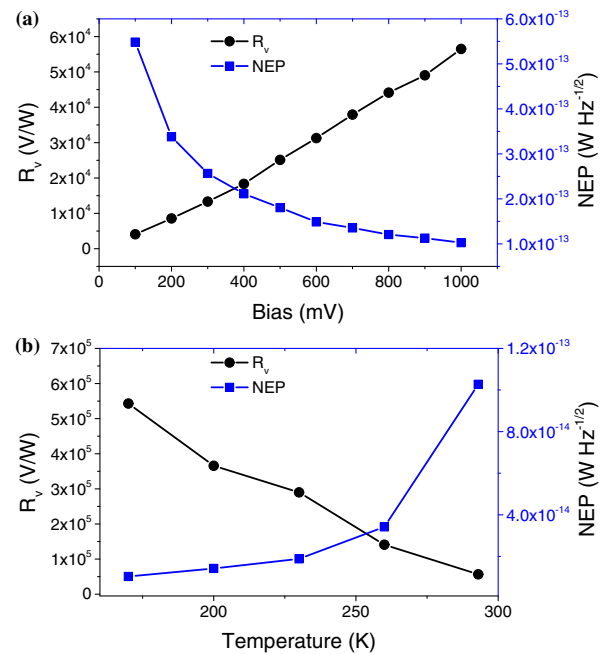


Fig. 5. Characterization of the detector at 0.270 THz. (a) Responsivity and NEP of the detector with respect to bias at 0.270 THz. (b) Responsivity and NEP of the detector with respect to temperature under an applied voltage bias of 1000 mV.

bias SBD (10^{-12} W Hz $^{-1/2}$ level) in the same band [36]. Temperature-dependent performance was characterized from room temperature (293 K) to thermoelectric cooling available at 170 K, shown in Fig. 5(b). As shown, the performance shows an overall improvement while decreasing the temperature. At 170 K, the R_v and NEP of the detector are 5.4×10^5 V W $^{-1}$ and 1.0×10^{-14} W Hz $^{-1/2}$, respectively, demonstrating an order of magnitude enhancement compared to those at room temperature. The same as an IR wave, such performance improvement can also be mainly ascribed to the increase in the electron mobility at low temperatures. It is noted here that we do not study the performance of our detector at extremely low temperatures because our interests are in uncooled or cheap thermoelectric cooling technologies. However, according to our previous report, the performance can be further improved while decreasing the temperature to 77 K [23].

The spectral response was characterized in Fig. 6 for a broad millimeter/terahertz wave range from 0.032 to 0.330 THz (or from K $_a$ to the W and G bands) limited by our facility. The detector exhibits a good photoresponse, as shown in Fig. 6(a), in all four bands (0.03–0.04 THz, 0.075–0.110 THz, 0.150–0.220 THz, and 0.225–0.330 THz). On the one hand, this can be ascribed to the broad spectral band coupling capability of the log-period antenna; on the other hand, it can be attributed to the negative permittivity of the InSb up to ~ 3 THz, as shown in Fig. 1(b). The multiple peak response character is caused by the multiple internal reflection from the substrate interface (or excitation of substrate modes), which can lead to an antenna pattern (gain and input impedance) degradation [37]. This problem can be solved by making the substrate thinner, using interconnection

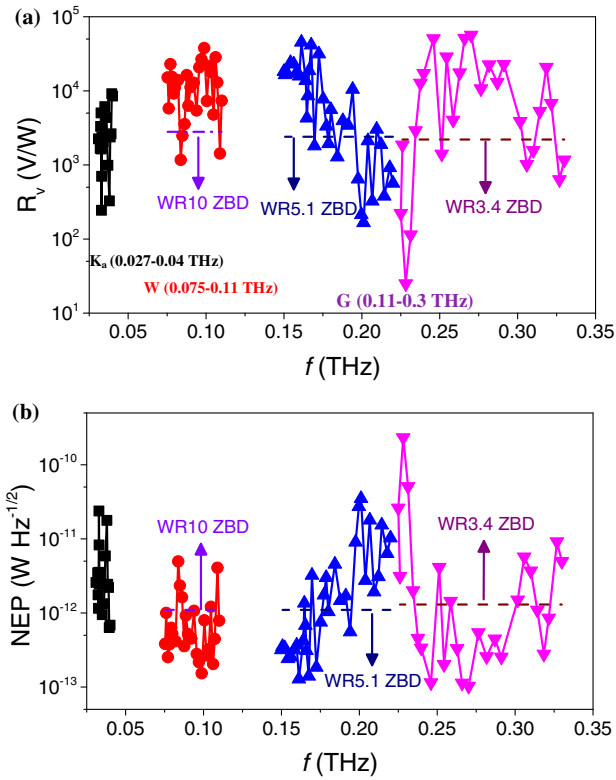


Fig. 6. Multispectral response of the detector for a millimeter/terahertz wave under an applied bias of 1000 mV. (a) Responsivity. (b) NEP. Performances of three commercial VDI modules are also plotted for comparison.

metallization, integrating a substrate lens, or using a conductive substrate [38–40]. The difference in the peak performance in the four bands may come from the difference in the coupling efficiency, as well as the difference in the conversion efficiency from coupled light to SPPs and from SPPs to nonequilibrium electrons. In Figs. 6(a) and 6(b), we also plot the typical R_v and NEP of state-of-the-art zero-bias diodes (ZBDs) in corresponding frequency bands. Note that the ZBD module is not available for the 0.03–0.04 THz/ K_a band [36]. As shown, our detector demonstrates an order of magnitude improvement within a broad spectral band. Therefore, we can conclude that using this type of single detector we achieve multiband millimeter/terahertz wave detection, which, in contrast, requires multiple modules for ZBD (WR10, WR5.1, and WR3.4, as denoted in Fig. 6). Specifically, at 0.270 THz (1.1 mm), the detector has R_v and NEP of $5.6 \times 10^4 \text{ V W}^{-1}$ and $1.0 \times 10^{-13} \text{ W Hz}^{-1/2}$, respectively. The performance only decreases slightly in the low frequency bands. For example, at 0.161 THz (1.86 mm), we achieve R_v and NEP of $4.5 \times 10^4 \text{ V W}^{-1}$ and $1.28 \times 10^{-13} \text{ W Hz}^{-1/2}$, respectively. Even at 0.039 THz (7.69 mm), the R_v and NEP of the detector can still reach $9.1 \times 10^3 \text{ V W}^{-1}$ and $6.3 \times 10^{-13} \text{ W Hz}^{-1/2}$, respectively. It is noted here that because the negative permittivity of InSb can hold until ~ 3 THz, our InSb detector is promising for even higher frequency band detection by engineering the coupling antenna; for example, by reducing the overall radius. We can also have an estimation on the D for

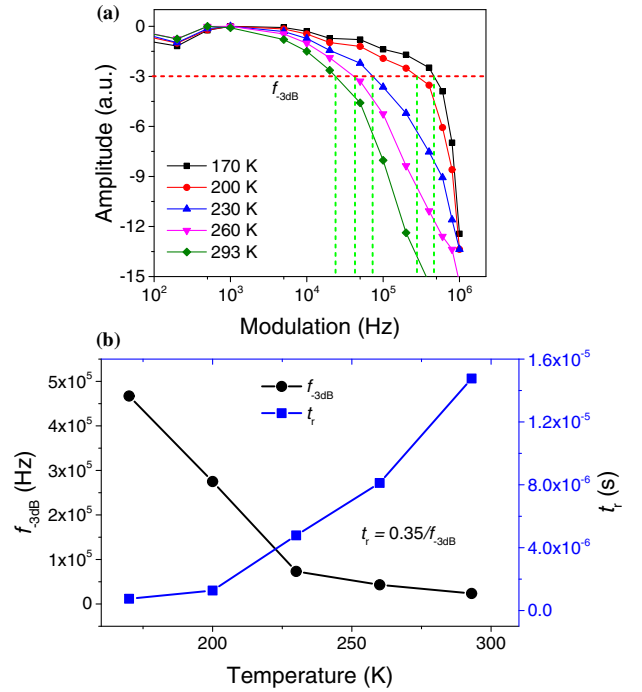


Fig. 7. Response speed of the detector for a millimeter/terahertz wave. (a) Normalized amplitude frequency response of the detector at 0.270 THz at different temperatures. (b) The $f_{-3\text{dB}}$ value and corresponding rise time of the detector derived from (a).

millimeter/terahertz wave as $D = A_e^{1/2}/\text{NEP}$, where A_e is the effective absorption area of the detector, as described above. At 0.270 THz, the D is about 8.3×10^{11} Jones.

We also characterized the response speed of the detector for millimeter/terahertz wave, as shown in Fig. 7. The typical amplitude frequency measurement is conducted with modulation up to 1 MHz at 0.270 THz, as shown in Fig. 7(a). The detector demonstrates an $f_{-3\text{dB}}$ bandwidth of 2.4×10^4 Hz for room-temperature operation, corresponding to a rise time of 1.5×10^{-5} s, as shown in Fig. 7(b). This is much faster than commercial Golay, pyroelectric, and uncooled semiconducting microbolometer detectors (ms level) [8]. But it is slower than metallic microbolometers, which possess a response speed faster than $\sim 3 \mu\text{s}$ [41–44]. It is also much slower than that of ZBDs, which can respond as fast as nanosecond level (GHz bandwidth). Nevertheless, the moderate response speed here can still meet the requirements for real-time imaging applications. The response speed of the detector is observed to become fast while decreasing the temperature. At 170 K, the corresponding $f_{-3\text{dB}}$ bandwidth and rise time are 4.7×10^5 Hz and 7.5×10^{-7} s, respectively, owing to the fast transition of nonequilibrium electrons at low temperatures [23]. The response speed of our detector for a millimeter/terahertz wave is probably governed by the decay time of SPPs, the lifetime of those nonequilibrium electrons, the time for photoconductive carriers to be collected by electrodes, and the RC factor in the whole measurement setup. Further study must be done to fully address this issue. A comparison of the performance of our detector with other solid-state technologies can be found in Table 1.

Table 1. Comparison of Uncooled Performance to State-of-the-Art Technologies for Millimeter/THz Wave

Technology	NEP ($\text{W Hz}^{-1/2}$)	Frequency (THz)	Speed (s)
Golay cells [9]	10^{-10} – 10^{-9}	0.02–30	$(2.5\text{--}5) \times 10^{-2}$
Pyroelectric [45]	10^{-9}	<30	10^{-1}
Schottky diodes [36]	10^{-12}	0.075–0.110 (WR10); 0.140–0.220 (WR5.1); 0.220–0.330 (WR3.4)	< 10^{-9}
Bolometers (HgCdTe, SiGe, Ti, NbN, VO _x , Nb, Al/Nb) [1]	10^{-11} – 10^{-9}	<3	10^{-6} – 10^{-3}
Si FET or Si CMOS [46,47]	10^{-11} – 10^{-10}	<0.7	–
CMOS-based (SiGe, GaAs/AlGaAs, InGaAs, InGaP/InGaAs/GaAs, GaN/AlGaN) [1]	10^{-11} – 10^{-9}	<3	–
Photoconductive antenna [3,48]	–	0.1–1.5 (depending on antenna)	< 10^{-9}
InAs/AlSb/AlGaSb [49]	1.8×10^{-13}	0.094	10^{-9}
AlGaIn/GaN [6]	5.8×10^{-13}	0.14	–
InAlAs/InGaAs/InP [50]	4.8×10^{-13}	0.2–0.292	–
InSb/AlInSb/GaSb/GaAs (this work)	1.0×10^{-13}	0.032–0.330	1.5×10^{-5}

As shown, our detector performs well compared to all of these technologies.

4. CONCLUSION

In conclusion, we present an epitaxially grown InSb on GaAs for multiband photodetection from IR to millimeter/terahertz wave. The detection for an IR wave is based on an interband transition in InSb, and a blackbody detectivity of 1.8×10^9 Jones is achieved with a cut-off wavelength of 6.85 μm at room temperature. By decreasing the temperature to thermoelectric cooling available at 170 K, the corresponding detectivity can be increased to 8.5×10^9 Jones with a blueshifted cut-off wavelength to 6.44 μm . For a millimeter/terahertz wave, the detector is equipped with a planar antenna and the photoresponse originates from the nonequilibrium electrons induced by SPPs. The detector achieves multiband detection from 0.032–0.040 THz (K_a band) to 0.075–0.110 THz (W band), and to 0.150–0.330 THz (G band). An NEP of 1.0×10^{-13} $\text{W Hz}^{-1/2}$ at 0.270 THz is demonstrated at room temperature and it is further reduced to as low as 1.0×10^{-14} $\text{W Hz}^{-1/2}$ at 170 K. The detector shows a moderate response speed for all frequency bands. Its overall performance is superior compared to current state-of-the-art technologies. Such detectors, capable of large scale and low cost, are promising for advanced uncooled multiband detection and imaging systems.

Funding. Agency for Science, Technology and Research (SERC 1720700038, SERC A1883c0002); Ministry of Education—Singapore (2017-T1-002-117).

Acknowledgment. J. Tong acknowledges support from Nanyang Technological University Presidential Postdoctoral Fellowship and help from Dr. Bingxuan Li, Dr. Gang Yih Chong, and Ms. Ling Ngo. The device fabrication was carried out at the Nanyang NanoFabrication Centre (N2FC).

Disclosures. The authors declare no conflicts of interest.

Data Availability. The data that support the findings of this paper are available within the paper.

REFERENCES

1. A. Rogalski, *Infrared and Terahertz Detectors*, 3rd ed. (CRC Press, 2019).
2. R. A. Lewis, "A review of terahertz detectors," *J. Phys. D* **52**, 433001 (2019).
3. K. Peng, P. Parkinson, L. Fu, Q. Gao, N. Jiang, Y.-N. Guo, F. Wang, H. J. Joyce, J. L. Boland, H. H. Tan, C. Jagadish, and M. B. Johnston, "Single nanowire photoconductive terahertz detectors," *Nano Lett.* **15**, 206–210 (2015).
4. K. Peng, D. Jevtics, F. Zhang, S. Sterzl, D. A. Damry, M. U. Rothmann, B. Guilhabert, M. J. Strain, H. H. Tan, L. M. Herz, L. Fu, M. D. Dawson, A. Hurtado, C. Jagadish, and M. B. Johnston, "Three-dimensional cross-nanowire networks recover full terahertz state," *Science* **368**, 510–513 (2020).
5. N. Wang, S. Cakmakyan, Y.-J. Lin, H. Javadi, and M. Jarrahi, "Room-temperature heterodyne terahertz detection with quantum-level sensitivity," *Nat. Astron.* **3**, 977–982 (2019).
6. H. W. Hou, Z. Liu, J. H. Teng, T. Palacios, and S. J. Chua, "High temperature terahertz detectors realized by a GaN high electron mobility transistor," *Sci. Rep.* **7**, 46664 (2017).
7. P. L. Richards, "Bolometers for IR and millimeter waves," *J. Appl. Phys.* **76**, 1–24 (1994).
8. F. Sizov, "Terahertz radiation detectors: the state-of-the-art," *Semicond. Sci. Technol.* **33**, 123001 (2018).
9. Tydex, "Golay detectors," http://www.tydexoptics.com/pdf/Golay_Detectors.pdf (accessed September 25, 2021).
10. A. Rogalski, M. Kopytko, and P. Martyniuk, "Two-dimensional infrared and terahertz detectors: outlook and status," *Appl. Phys. Rev.* **6**, 021316 (2019).
11. Q. Qiu and Z. Huang, "Photodetectors of 2D materials from ultraviolet to terahertz waves," *Adv. Mater.* **33**, 2008126 (2021).
12. V. Giannini, A. Berrier, S. A. Maier, J. A. Sánchez-Gil, and J. G. Rivas, "Scattering efficiency and near field enhancement of active semiconductor plasmonic antennas at terahertz frequencies," *Opt. Express* **18**, 2797–2807 (2010).
13. L. Deng, J. Teng, H. Liu, Q. Y. Wu, J. Tang, X. Zhang, S. A. Maier, K. P. Lim, C. Y. Ngo, S. F. Yoon, and S. J. Chua, "Direct optical tuning of the terahertz plasmonic response of InSb subwavelength gratings," *Adv. Opt. Mater.* **1**, 128–132 (2013).
14. S. M. Hanham, A. I. Fernández-Domínguez, J. H. Teng, S. S. Ang, K. P. Lim, S. F. Yoon, C. Y. Ngo, N. Klein, J. B. Pendry, and S. A. Maier, "Broadband terahertz plasmonic response of touching InSb disks," *Adv. Mater.* **24**, OP226–OP230 (2012).
15. R. Parthasarathy, A. Bykhovski, B. Gelmont, T. Globus, N. Swami, and D. Woolard, "Enhanced coupling of subterahertz radiation with semiconductor periodic slot arrays," *Phys. Rev. Lett.* **98**, 153906 (2007).
16. G. Jaime, C. Janke, P. H. Bolivar, and H. Kurz, "Transmission of THz radiation through InSb gratings of subwavelength apertures," *Opt. Express* **13**, 847–859 (2005).

17. R. Sundararaman, P. Narang, A. S. Jermyn, W. A. Goddard III, and H. A. Atwater, "Theoretical predictions for hot-carrier generation from surface plasmon decay," *Nat. Commun.* **5**, 5788 (2014).
18. C. Clavero, "Plasmon-induced hot-electron generation at nanoparticle/metal-oxide interfaces for photovoltaic and photocatalytic devices," *Nat. Photonics* **8**, 95–103 (2014).
19. J. Lehmann, M. Merschorf, W. Pfeiffer, A. Thon, S. Voll, and G. Gerber, "Surface plasmon dynamics in silver nanoparticles studied by femtosecond time-resolved photoemission," *Phys. Rev. Lett.* **85**, 2921–2924 (2000).
20. K. Wu, J. Chen, J. R. McBride, and T. Lian, "Efficient hot-electron transfer by a plasmon-induced interfacial charge-transfer transition," *Science* **349**, 632–635 (2015).
21. M. W. Knight, H. Sobhani, P. Nordlander, and N. J. Halas, "Photo-detection with active optical antennas," *Science* **332**, 702–704 (2011).
22. A. Giugni, B. Torre, A. Toma, M. Francardi, M. Malerba, A. Alabastri, R. Proietti Zaccaria, M. I. Stockman, and E. Di Fabrizio, "Hot-electron nanoscopy using adiabatic compression of surface plasmons," *Nat. Nanotechnol.* **8**, 845–852 (2013).
23. J. Tong, W. Zhou, Y. Qu, Z. Xu, Z. Huang, and D. H. Zhang, "Surface plasmon induced direct detection of long wavelength photons," *Nat. Commun.* **8**, 1660 (2017).
24. J. Tong, F. Suo, T. Zhang, Z. Huang, J. Chu, and D. H. Zhang, "Plasmonic semiconductor nanogroove array enhanced broad spectral band millimetre and terahertz wave detection," *Light Sci. Appl.* **10**, 58 (2021).
25. C. Balanis, *Antenna Theory: Analysis and Design*, 4th ed. (Wiley, 2016).
26. R. DuHamel and F. Ore, "Logarithmically periodic antenna designs," in *IRE International Convention Record* (Institute of Electrical and Electronics Engineers, 2005), Vol. 6, pp. 139–151.
27. L. Vicarelli, M. S. Vitiello, D. Coquillat, A. Lombardo, A. C. Ferrari, W. Knap, M. Polini, V. Pellegrini, and A. Tredicucci, "Graphene field-effect transistors as room-temperature terahertz detectors," *Nat. Mater.* **11**, 865–871 (2012).
28. L. Viti, J. Hu, D. Coquillat, W. Knap, A. Tredicucci, A. Politano, and M. S. Vitiello, "Black phosphorus terahertz photodetectors," *Adv. Mater.* **27**, 5567–5572 (2015).
29. Y. Li, Y. Zhang, T. Li, M. Li, Z. Chen, Q. Li, H. Zhao, Q. Sheng, W. Shi, and J. Yao, "Ultrabroadband, ultraviolet to terahertz, and high sensitivity $\text{CH}_3\text{NH}_3\text{PbI}_3$ perovskite photodetectors," *Nano Lett.* **20**, 5646–5654 (2020).
30. Y. Chen, Y. Wang, Z. Wang, Y. Gu, Y. Ye, X. Chai, J. Ye, Y. Chen, R. Xie, Y. Zhou, Z. Hu, Q. Li, L. Zhang, F. Wang, P. Wang, J. Miao, J. Wang, X. Chen, W. Lu, P. Zhou, and W. Hu, "Unipolar barrier photo-detectors based on van der Waals heterostructures," *Nat. Electron.* **4**, 357–363 (2021).
31. Y. Fang, A. Armin, P. Meredith, and J. Huang, "Accurate characterization of next-generation thin-film photodetectors," *Nat. Photonics* **13**, 1–4 (2019).
32. Hamamatsu Photonics, "InSb photoconductive detectors," <https://www.hamamatsu.com/jp/en/product/optical-sensors/infrared-detector/insb-photovoltaic-detector.html> (accessed September 25, 2021).
33. Hamamatsu Photonics, "InAsSb photovoltaic detectors," https://www.hamamatsu.com/resources/pdf/ssd/p13243_series_kird1130e.pdf (accessed September 25, 2021).
34. Thorlabs, "Mid-IR photovoltaic detectors, HgCdTe (MCT)," https://www.thorlabs.com/newgrouppage9.cfm?objectgroup_id=11319 (accessed September 25, 2021).
35. J. Yan, M. H. Kim, J. A. Elle, A. B. Sushkov, G. S. Jenkins, H. M. Milchberg, M. S. Fuhrer, and H. D. Drew, "Dual-gated bilayer graphene hot-electron bolometer," *Nat. Nanotechnol.* **7**, 472–478 (2012).
36. Virginia Diodes, Inc., "Detectors," <https://www.vadiodes.com/en/products/detectors> (accessed September 26, 2021).
37. D. Pozar, "Considerations for millimeter wave printed antennas," *IEEE Trans. Antennas Propag.* **31**, 740–747 (1983).
38. A. Dhiflaoui, A. Yahyaoui, J. Youssaf, T. Aguilu, B. Hakim, H. Rmili, and R. Mittra, "Full wave numerical analysis of wideband and high directive log spiral THz photoconductive antenna," *Int. J. Numer. Model. Electron. Netw. Devices Fields* **33**, e2761 (2020).
39. M. Sakhno, J. Gumenjuk-Sichevska, and F. Sizov, "Modeling of the substrate influence on multielement THz detector operation," *J. Infrared Millim. Terahertz Waves* **35**, 703–719 (2014).
40. T. K. Nguyen, T. A. Ho, H. Han, and I. Park, "Numerical study of self-complementary antenna characteristics on substrate lenses at terahertz frequency," *J. Infrared Millim. Terahertz Waves* **33**, 1123–1137 (2012).
41. E. N. Grossman and A. J. Miller, "Active millimeter-wave imaging for concealed weapons detection," *Proc. SPIE* **5077**, 62 (2003).
42. X.-C. Tu, L. Kang, X.-H. Liu, Q.-K. Mao, C. Wan, J. Chen, B.-B. Jin, Z.-M. Ji, W.-W. Xu, and P.-H. Wu, " Nb_3N_6 microbolometer arrays for terahertz detection," *Chin. Phys. B* **22**, 040701 (2013).
43. I. Kašalynas, R. Venckevičius, L. Minkevičius, A. Sešek, F. Wahaia, V. Tamošiūnas, B. Voisiat, D. Seliuta, G. Valušis, A. Švigelj, and J. Trontelj, "Spectroscopic terahertz imaging at room temperature employing microbolometer terahertz sensors and its application to the study of carcinoma tissues," *Sensors* **16**, 432 (2016).
44. D. Rutledge and S. Schwarz, "Planar multimode detector arrays for infrared and millimeter-wave applications," *IEEE J. Quantum Electron.* **17**, 407–414 (1981).
45. QMC Instruments Ltd., "Terahertz pyroelectric detectors," <http://www.terahertz.co.uk/qmc-instruments-ltd/thz-detector-systems/pyroelectric-detectors> (accessed September 25, 2021).
46. R. Tauk, F. Teppe, S. Boubanga, D. Coquillat, W. Knap, Y. M. Meziani, C. Gallon, F. Boeuf, T. Skotnicki, C. Fenouillet-Beranger, D. K. Maude, S. Rumyantsev, and M. S. Shur, "Plasma wave detection of terahertz radiation by silicon field effects transistors: responsivity and noise equivalent power," *Appl. Phys. Lett.* **89**, 253511 (2006).
47. U. R. Pfeiffer and E. Ojefors, "Terahertz imaging with CMOS/BiCMOS process technologies," in *Proceedings of European Solid State Circuits Conference (ESSCIRC)* (IEEE, 2010), pp. 52–60.
48. E. Castro-Camus, J. Lloyd-Hughes, M. B. Johnston, M. D. Fraser, H. H. Tan, and C. Jagadish, "Polarization-sensitive terahertz detection by multicontact photoconductive receivers," *Appl. Phys. Lett.* **86**, 254102 (2005).
49. Z. Zhang, R. Rajavel, P. Deelman, and P. Fay, "Sub-micron area heterojunction backward diode millimeter-wave detectors with $0.18 \text{ pW/Hz}^{1/2}$ noise equivalent power," *IEEE Microw. Wirel. Components Lett.* **21**, 267–269 (2011).
50. Y. Kurita, G. Ducournau, D. Coquillat, A. Satou, K. Kobayashi, S. B. Tombet, Y. M. Meziani, V. V. Popov, W. Knap, T. Suemitsu, and T. Otsuji, "Ultrahigh sensitive sub-terahertz detection by InP-based asymmetric dual-grating-gate high-electron-mobility transistors and their broadband characteristics," *Appl. Phys. Lett.* **104**, 251114 (2014).